

# Variable Carrier Phase Shift Method for Integrated Contactless Field Excitation System of Electrically Excited Synchronous Motors

Enes Ayaz, Oğün Altun, Ozan Keysan

**Abstract**—This paper presents a novel contactless field excitation (CFE) system based on wireless power transfer (WPT), which utilizes the existing voltage source inverter (VSI) of the motor drive for electrically excited synchronous motors (EESMs). In conventional CFE systems, an extra high-frequency converter is required to excite the field winding. In this paper, it is proposed to utilize existing voltage switching harmonics of the VSI for exciting the field winding while the low-frequency modulated component is used to drive the motor. In the proposed system, a novel variable carrier phase shift method (VCPSM) is developed to achieve constant input excitation voltage for the WPT part independently from the motor operation. In addition, a hybrid frequency detuning control method is introduced to adjust the field current. For experimental validation, a small-scale prototype with 100 V DC-link and 60 kHz switching frequency is established. It is observed that the field current could be kept almost constant at 5 A under different motor driving conditions operations regarding modulation index and fundamental frequency. Also, it is shown that the field current could be reduced by detuning the switching frequency. In brief, without an additional active converter and only with a software update, a cost-effective CFE system for EESMs can be easily implemented.

**Index Terms**—Contactless field excitation, wireless power transfer, motor drive, SPWM, carrier phase shift

## I. INTRODUCTION

The interest of the automotive industry is continuously increasing in electric vehicles (EVs) or hybrid electric vehicles (HEVs) rather than internal combustion engine vehicles (ICEVs) [1]. One of the critical parts of EVs and HEVs is the traction system, where permanent magnet synchronous motors (PMSMs) are commonly preferred due to their high torque density [2]. However, high cost and limited supply of rare-earth magnets such as Neodymium (Nd) and Samarium (Sm) encourage less-PM or no-PM motors such as electrically excited synchronous motors (EESMs) [3]–[6]. EESMs can decrease the total cost and have flexible control thanks to their externally excited field windings [7], [8]. Moreover, they are more reliable as the demagnetization of PMs due to high temperature is not an issue in EESMs. However, power transfer to their rotating field windings is challenging.

This work has been submitted to the IEEE for possible publication. Copyright may be transferred without notice, after which this version may no longer be accessible.

Enes Ayaz, Oğün Altun, and Ozan Keysan are with the Department of Electrical and Electronics Engineering, Middle East Technical University, Ankara, Turkey

Corresponding Author: Ozan Keysan, keysan@metu.edu.tr

The most common method to excite field windings is to use slip rings with conductor rings and carbon brushes. Although slip rings are a mature and cost-effective technology, they require periodic maintenance due to the wear of the brushes [9]. Another method is to use brushless exciters that are, in fact, synchronous generators (SGs) with rotating rectifiers. However, this method is not applicable for variable speed drives such as in EVs [10]. Alternative to these methods, contactless field excitation (CFE) systems based on wireless power transfer (WPT) are proposed as shown in Fig. 1.a [11]–[15]. They have no physical contact between the rotating and stationary frames, eliminating the maintenance issue. However, extra high-frequency converter increases the cost and complexity.

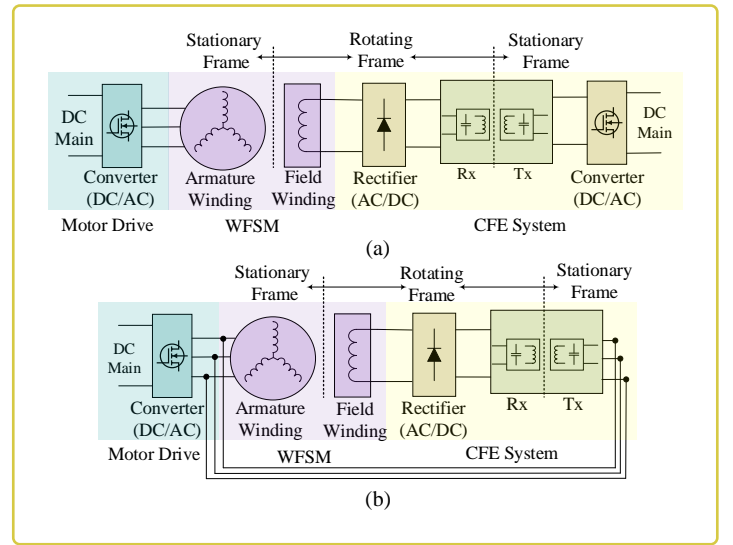


Fig. 1. The circuit diagram of a conventional and the proposed CFE based on a WPT system for EESMs. a) The conventional system. b) The proposed system.

The VSI of the motor drive generates a low-frequency modulated voltage with high-frequency switching harmonics. This low-frequency modulated voltage controls the speed and torque of the motor, whereas the motor windings filter out the high-frequency voltage harmonics thanks to high phase inductances. In this paper, it is proposed that these high-frequency harmonics of the existing converter of the motor drive can be used to energize the field winding while the low-frequency modulated voltage can still be used to drive the motor. The proposed system is shown in Fig. 1.b.

Motor drives use modulation techniques such as sinusoidal pulse width modulation (SPWM) or space-vector pulse width modulation (SVPWM). Yet, these modulation techniques affect the content of the high-frequency switching harmonics in addition to controlling the low-frequency modulated voltage. Therefore, an independent control algorithm for the high-frequency switching harmonic components is required. In this study, a novel variable carrier phase-shift method (VCPSM) is proposed to achieve independent field current control while driving the motor. The main advantage of the proposed method is that it can be applied in conventional motor drives by just updating the software, so the system can be easily implemented without extra cost.

The rest of the paper is organized as follows. Section II presents the system structure and defines the problem. Section III proposes the variable carrier phase shift method and control strategy of the field current. Section IV gives the WPT system's design stage regarding the proposed method's restriction. Section V presents the experimental results.

## II. SYSTEM STRUCTURE AND PROBLEM DEFINITION

The proposed system aims for an integrated contactless field excitation system for electrically excited synchronous motors of EVs. A 2-level voltage source inverter (VSI) is the most common topology in commercial EV drives [16]. In the past, discrete IGBTs or module IGBTs have been used with their switching frequencies around 20 kHz [17]. Since the wireless power transfer systems become bulky in this frequency range, the proposed integrated CFE system is not feasible. However, in recent years, wide band-gap semiconductors such as SiC MOSFETs or GaN HEMTs are becoming more popular in the automotive industry [18]. Thanks to their high switching frequencies up to 100 kHz, the passive components can be shrunk [19]. Similarly, a higher switching frequency reduces the size of the transmitter and receiver coils of the WPT system and makes the proposed integrated CFE system more feasible.

Several topologies, such as capacitive power transfer (CPT) and inductive power transfer (IPT), can be used in CFE systems [20]–[28]. Reducing the size of the system is essential as the system should fit inside the motor. Therefore, the IPT system is chosen thanks to its wide range of frequency, power, and smaller size. In IPT systems, Tx and Rx coils are loosely coupled, resulting in inherently low power factors. Therefore, compensation circuits are generally used [29]–[31]. Series compensation is preferred in the Tx coil as a VSI is used in motor drives. Besides, the Rx side compensation is not used since achieving a lightweight and small volume on the rotating side is desired in the proposed system.

In the remaining parts of the paper, a series-none (SN) topology is selected, and a 2-level 3-phase 3-wire ( $3\Phi\text{-}3\text{W}$ ) VSI (driven by SPWM) is used, although the proposed system can be adapted to different converters, modulation techniques, or WPT systems.

### A. Problem Definition

Conventional WPT systems have two wire inputs, and motor drives have 3-wire outputs so that the WPT system can be

connected between any two of three phases, as given in Fig. 2. In this configuration (the WPT system will be connected

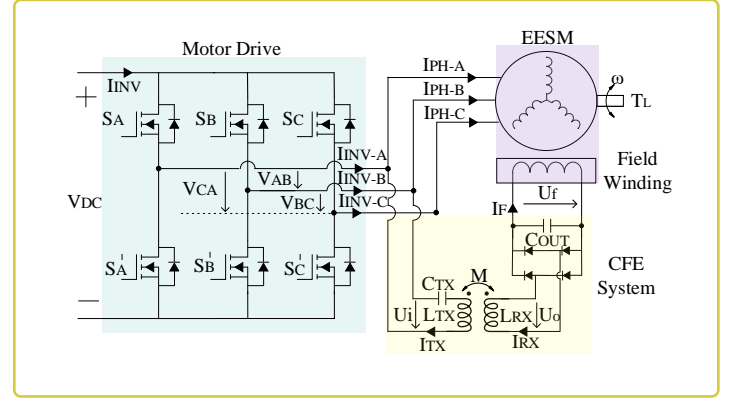


Fig. 2. The circuit diagram of the proposed system.

between legs A and B), the excitation voltage of the WPT system ( $U_i(t)$ ) can be calculated as in (1)

$$U_i(t) = V_{DC} S_{AB}(t) = V_{DC} (S_A(t) - S_B(t)) \quad (1)$$

where the switching function (of leg A or leg B) is calculated by double Fourier series for SPWM as shown in (2), which has been analyzed in [32].

$$\begin{aligned} S_{(A,B)}(t) = & \frac{1}{2} + \frac{m_a}{2} \cos \left( \omega_o t + \theta_{o(A,B)} \right) \\ & + \frac{2}{\pi} \sum_{i=1}^{i=\infty} \left[ J_o \left( i \frac{\pi}{2} m_a \right) \sin \left( i \frac{\pi}{2} \right) \right. \\ & \quad \left. \cos \left( i [\omega_c t + \phi_{c_{(A,B)}}] \right) \right] \\ & + \frac{2}{\pi} \sum_{i=1}^{i=\infty} \sum_{k=-\infty}^{k=\infty} \left[ \frac{1}{i} J_k \left( i \frac{\pi}{2} m_a \right) \sin \left( (i+k) \frac{\pi}{2} \right) \right. \\ & \quad \left. \cos \left( i [\omega_c t + \phi_{c_{(A,B)}}] + k [\omega_o t + \theta_{o(A,B)}] \right) \right] \end{aligned} \quad (2)$$

According to (2), the harmonic distribution of SPWM changes with modulation index as shown in Fig. 3. Although several components exist, such as DC, fundamental, switching, and sideband harmonics, only the first switching harmonic and its sideband components (denoted by  $U_i^f(t)$ ) dominate in the WPT system since the WPT system behaves like a bandpass filter characteristic, and its resonant frequency is tuned to near the switching frequency. Therefore, only  $U_i^f(t)$  can be used in the mathematical model. The first switching harmonic and its sideband components [ $S_{(A,B)}^{f_s}(t)$ ,  $S_{(A,B)}^{f_s-2f_o}(t)$ , and  $S_{(A,B)}^{f_s+2f_o}(t)$ ] of the switching function can be calculated as in (3,4,5) by taking  $(i = 1)$ ,  $(i = 1, k = -2)$ , and  $(i = 1, k = 2)$  in (2), respectively.

$$S_{(A,B)}^{f_s}(t) = \frac{2}{\pi} J_0(m_a \frac{\pi}{2}) \cos(2\pi(f_s)t + \phi_{c_{(A,B)}}) \quad (3)$$

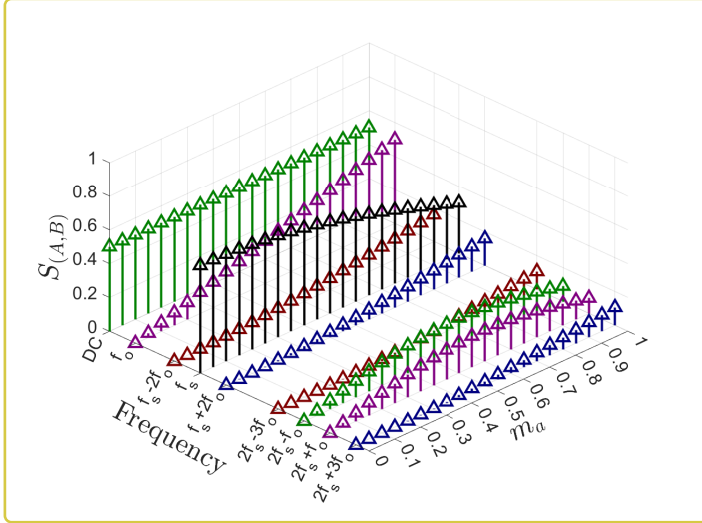


Fig. 3. The harmonic distribution of SPWM for varying modulation index.

$$S_{(A,B)}^{f_s-2f_o}(t) = \frac{2}{\pi} J_2(m_a \frac{\pi}{2}) \cos \left( +\phi_{c(A,B)} - 2\theta_{o(A,B)} \right) \quad (4)$$

$$S_{(A,B)}^{f_s+2f_o}(t) = \frac{2}{\pi} J_2(m_a \frac{\pi}{2}) \cos \left( +\phi_{c(A,B)} + 2\theta_{o(A,B)} \right) \quad (5)$$

After that,  $U_i^f$  can be calculated as in (6) by subtracting the switching and its sideband harmonics of leg B from those of leg A.

In conventional SPWM, each phase uses the same carrier signals, which means that  $\phi_{CA} = \phi_{CB}$ . Hence, according to (6), the switching frequency disappears in  $U_i^f(t)$ , and just only its sidebands exist.  $U_i(t)$  and  $U_i^f(t)$  are plotted in Fig. 4 for different modulation indices. It is observed that  $U_i^f(t)$  increases with the modulation index, and zero voltage (zero excitation) occurs at some moments. These zero excitation instants create low-frequency power fluctuations that disrupt constant power transfer. Therefore, a control method is required to achieve a continuous/constant power transfer at the switching harmonic for the WPT system without disturbing the fundamental component. However, conventional control methods of the WPT system are not suitable for this. A conventional method is to control the duty cycle, but this also affects the fundamental component. Another method is frequency detuning control, but it cannot guarantee continuous power transfer since zero voltage moments exist, indicated via red arrows in Fig. 4. The last method is to add a post-

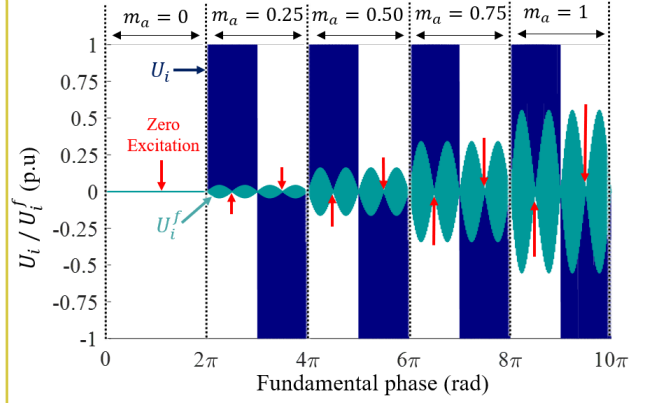


Fig. 4. The normalized input excitation voltage waveforms of the WPT system. Zero voltage points at input excitation voltage are indicated by red arrows.

regulation converter or use an active rectifier at the output of the WPT system. However, this increases the system's cost and complexity, and the problem of zero voltage moments still exists. In this paper, a new control method, introducing variable carrier phase shift, is proposed to avoid zero voltage moments and achieve continuous power transfer for changing modulation indices.

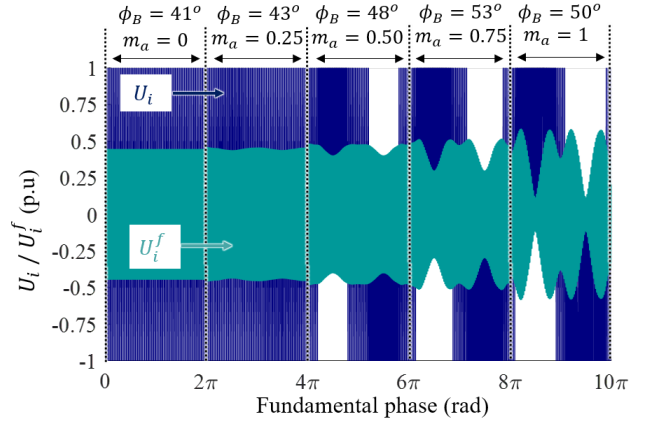


Fig. 5. The normalized input excitation voltage waveforms of the WPT system.

The proposed method is similar to a dual-frequency power transfer system with a single converter [33]–[37]. In [34], a single-inverter-based dual-frequency WPT system is proposed using the programmed PWM method. However, the programmed PWM method is computationally complex and requires switching angle calculations using offline algorithms, which is not feasible in dynamic systems such as our cases. In [35], [36], multi-frequencies are achieved by comparing su-

$$\begin{aligned} \frac{U_i^f(t)}{V_{DC}} &= \frac{2}{\pi} J_2 \left( m_a \frac{\pi}{2} \right) \cos \left( 2\pi(f_s - 2f_o)t + \phi_A - 2\theta_A \right) - \frac{2}{\pi} J_2 \left( m_a \frac{\pi}{2} \right) \cos \left( 2\pi(f_s - 2f_o)t + \phi_B - 2\theta_B \right) + \frac{2}{\pi} J_0 \left( m_a \frac{\pi}{2} \right) \cos \left( 2\pi(f_s)t + \phi_A \right) \\ &\quad - \frac{2}{\pi} J_0 \left( m_a \frac{\pi}{2} \right) \cos \left( 2\pi(f_s)t + \phi_B \right) + \frac{2}{\pi} J_2 \left( m_a \frac{\pi}{2} \right) \cos \left( 2\pi(f_s + 2f_o)t + \phi_A + 2\theta_A \right) - \frac{2}{\pi} J_2 \left( m_a \frac{\pi}{2} \right) \cos \left( 2\pi(f_s + 2f_o)t + \phi_B + 2\theta_B \right) \end{aligned} \quad (6)$$

perimposed sinusoidal reference signals with a high-frequency triangular carrier signal. However, in these methods, the switching frequency is higher than the operating frequencies of the WPT system, which increases the switching losses. In [37], multi-frequency components are achieved by a multi-level inverter (MLI) with a switching frequency lower than its two-level alternatives. However, this system uses a higher number of switching components, which is actually the opposite of the main proposal. In [38], a carrier-phase shift (CPS) method is proposed to control the switching harmonic independently. The amount of the CPS is determined according to the modulation index. Since a constant CPS is applied until the modulation index changes, a low-frequency ripple exist there.

The low-frequency fluctuation is seen in Fig. 5. Although the low-frequency fluctuation may be acceptable in rotating loads and can be reduced by increasing the output capacitance, it should be mitigated in the application of the field excitation system since it also creates a torque and speed ripple in the motor. In order to solve this problem, the variable carrier phase shift method (VCPSM) is proposed. This method calculates and updates the carrier phase shift for each duty cycle change rather than updating the modulation.

### III. THE PROPOSED VARIABLE CARRIER PHASE SHIFT METHOD (VCPSM) AND FIELD CURRENT REGULATION

The variable carrier phase shift method aims to achieve a constant switching harmonic during each switching interval. In this section, firstly, a mathematical model is developed for SPWM. Then, the selection of the magnitude of the switching component is discussed. Finally, the regulation strategy of the field current is presented.

#### A. Mathematical Modelling

Fig. 6 shows the SPWM technique with reference, carrier, and PWM signals, where different carrier signals (implying that  $\phi_{cA} \neq \phi_{cB} \neq \phi_{cC}$ ) are used for each phase. The duty cycle of each phase ( $D_A, D_B, D_C$ ) follows its corresponding reference signal, as given in (7). In other words, square waves with varying duty cycles are generated within a switching interval. The duty cycles depend on the reference signals, as given in (7), and the phases of the square waves change with the phases of the carrier signals, as can be observed in Fig. 6. The first switching harmonic components for these square waves can be calculated using the Fourier series, as given in (8).

$$\begin{aligned} D_A &= \sin(2\pi f_{ot}) \\ D_B &= \sin(2\pi f_{ot} - \frac{2\pi}{3}) \\ D_C &= \sin(2\pi f_{ot} + \frac{2\pi}{3}) \end{aligned} \quad (7)$$

$$\begin{aligned} S_A(t)^{f_s} &= \frac{2}{\pi} \sin(\pi D_A) \cos(2\pi f_{st} t + \phi_{cA}) \\ S_B(t)^{f_s} &= \frac{2}{\pi} \sin(\pi D_B) \cos(2\pi f_{st} t + \phi_{cB}) \\ S_C(t)^{f_s} &= \frac{2}{\pi} \sin(\pi D_C) \cos(2\pi f_{st} t + \phi_{cC}) \end{aligned} \quad (8)$$

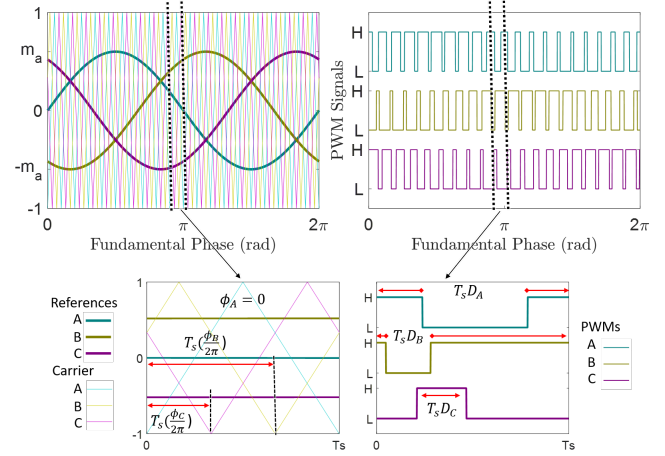


Fig. 6. The key waveforms of SPWM. For visual clarity, the switching frequency is decreased.

Then, the normalized magnitude of the switching component for the phase-to-phase connection can be calculated as in (9). Therefore, the magnitude of the switching harmonic can be calculated in phasor domain as in (10) by taking the difference between two phasors.

$$\begin{aligned} S_{AB}(t)^{f_s} &= S_A(t)^{f_s} - S_B(t)^{f_s} \\ &= \frac{2}{\pi} \sin(\pi D_A) \cos(2\pi f_{st} t + \phi_{cA}) \\ &\quad - \frac{2}{\pi} \sin(\pi D_B) \cos(2\pi f_{st} t + \phi_{cB}) \end{aligned} \quad (9)$$

$$\hat{S}_{AB,f_s} = \frac{2}{\pi} \sqrt{\frac{\sin(\pi D_A)^2 + \sin(\pi D_B)^2}{-2(\sin(\pi D_A)(\sin(\pi D_B)\cos(\phi_{cA} - \phi_{cB}))}} \quad (10)$$

Consequently, the magnitude of the switching component can be adjusted by introducing a phase shift between the carrier signals, and the required carrier-phase-shift value to keep  $\hat{S}_{AB,f_s}$  constant at the desired value can be calculated using (9), and found as given in (11).

$$\begin{aligned} \phi_{CPS} &= \phi_{cA} - \phi_{cB} = \\ &\cos^{-1} \left[ \frac{\sin(\pi D_A)^2 + \sin(\pi D_B)^2 - (\frac{\pi}{2} \hat{S}_{AB,f_s})^2}{2 \sin(\pi D_A) \sin(\pi D_B)} \right] \end{aligned} \quad (11)$$

However, it should be considered that the amount of carrier phase shift is restricted between  $0^\circ$  and  $180^\circ$ , which gives the minimum and maximum  $\hat{S}_{AB,f_s}$ . Besides,  $D_A$  and  $D_B$  are not independent variables, and they follow the reference signals. Therefore, the reachable  $\hat{S}_{AB,f_s}$  is restricted and changes regarding the parameters of  $D_A$ ,  $D_B$ , and  $\phi_{CPS}$ . For these reasons, the selection of  $\hat{S}_{AB,f_s}$  that is independent of the modulation index is challenging.

#### B. Selection of $\hat{S}_{AB,f_s}$

According to phasor calculation in (10), the maximum and minimum values of  $\hat{S}_{AB,f_s}$  should be complied by triangle

inequality, as given in (12).

$$\begin{aligned} \frac{2}{\pi} |\sin(\pi D_A) - \sin(\pi D_B)| &< \hat{S}_{AB_{fs}} \\ &< \frac{2}{\pi} |\sin(\pi D_A) + \sin(\pi D_B)| \end{aligned} \quad (12)$$

Hence, these maximum and minimum values change according to modulation indices, as shown in Fig. 7.

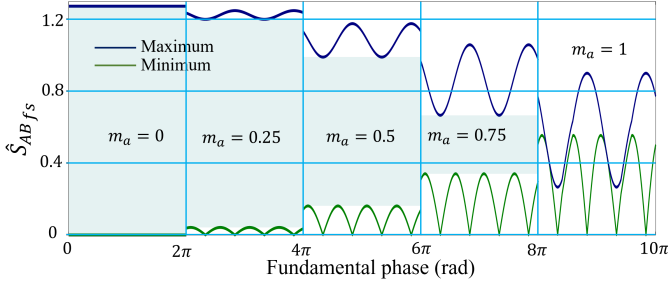


Fig. 7. The minimum and maximum normalized input excitation voltage limits for the proposed method under several modulation indices. The reachable excitation voltages are indicated by turquoise.

The aim is to achieve a constant  $\hat{S}_{AB_{fs}}$  for any motor operation. However, it is observed that the range of the allowed  $\hat{S}_{AB_{fs}}$  is reduced by increasing the modulation index, and it may not guarantee a constant value for a higher modulation index. The allowed  $\hat{S}_{AB_{fs}}$  values are plotted along modulation indices in Fig. 8.

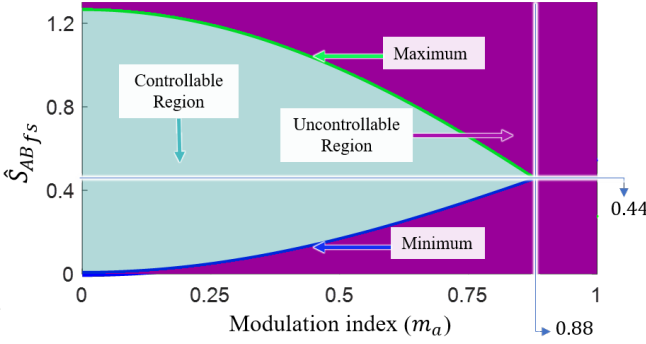


Fig. 8. Controllable and uncontrollable regions of the proposed method regarding modulation index.

The allowed range of the WPT system is inversely proportional to the range of the motor drive control. For example,  $\hat{S}_{AB_{fs}}$  can be controlled between 0.30 and 0.60 for the modulation index below 0.6. Therefore, if a higher  $\hat{S}_{AB_{fs}}$  is desired, the modulation index of the motor drive should be restricted to a lower value, which also decreases the DC-link utilization. However, the selection of  $\hat{S}_{AB_{fs}}$ , DC-link voltage, and modulation index are related to the system requirements. In this study, as a proof of concept, the  $\hat{S}_{AB_{fs}}$  limit is selected at 0.44, where the motor operation should be restricted to a maximum modulation index of 0.8.

### C. Field Current Regulation

In the proposed method, the power of the WPT system is not directly controlled, but it only guarantees to keep the input excitation voltage at a constant value. Therefore, a control strategy for the field current should be developed. Several conventional methods are used in WPT systems, such as duty cycle control and post-regulation converter (or active rectifier). The duty cycle control is unsuitable for cooperating with the proposed method since it also changes the fundamental component. A post-regulation converter could be used, but it is not preferred as it increases the cost and complexity of the system. Alternatively, the frequency detuning method that controls the gain of the WPT system can be used, which does not require extra hardware and is simple to implement, so it is preferred in the proposed system. Accordingly, the overall control block diagram of the hybrid control strategy consisting of frequency detuning and variable carrier phase shift methods is presented in Fig. 9.

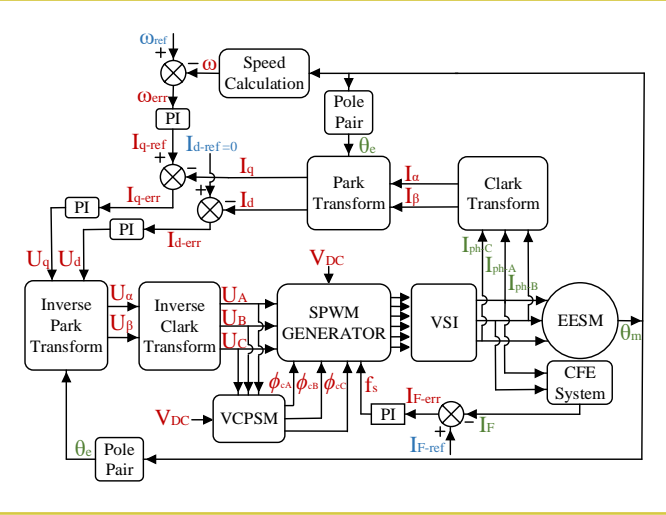


Fig. 9. The control scheme of the proposed CFE system. References are in blue, measurements are in green, and control parameters and calculations are in red.

A conventional PI controller can be used to regulate the current and speed of the motor. The proposed VCPSM algorithm calculates the carrier phases based on the duty cycles generated by this conventional PI controller. An additional PI controller regulates the field current by varying the switching frequency. Consequently, duty cycles, carrier phases, and switching frequency are used as input parameters for SPWM, and a VSI, governed by this SPWM, generates voltage waveforms to drive the motor.

## IV. THE DESIGN OF THE SN-WPT SYSTEM

This section will first analyze the series-none (SN) compensated WPT system and then present the system's design steps as a guideline.

### A. Analysis of the SN-WPT System

The analysis of the SN-WPT system is similar to that of the LLC converter [39]. The circuit diagram of the SN-WPT system is shown in Fig. 10.a. The first harmonic approximation (FHA) can be used to analyze this system, as illustrated in Fig. 10.b.

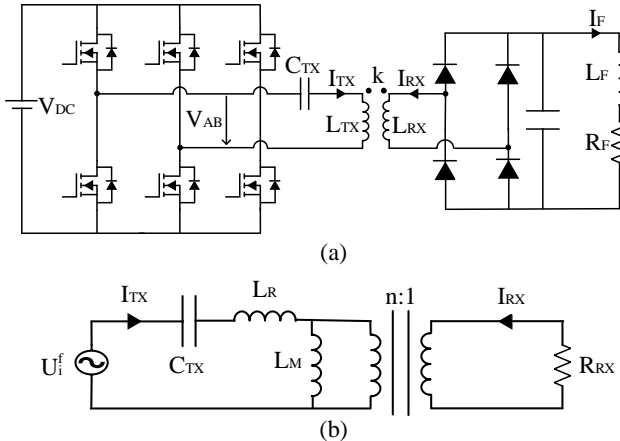


Fig. 10. a) The circuit diagram of the SN-WPT system with 3-phase VSI. b) FHA-based transformer modeling of SN-WPT system.

In this system, the Tx-side capacitance is used to compensate for the leakage inductance, which is termed as  $L_R$ . Therefore, the output voltage depends on the transformer turns ratio and input voltage at the resonant frequency as given in (13).

$$U_o = \frac{U_i}{n} \quad (13)$$

Besides, the resonant frequency  $f_r$  is determined by the compensation capacitance, which is presented in (14).

$$f_r = \frac{1}{2\pi\sqrt{L_R C_{Tx}}} \quad (14)$$

Moreover, the transformer modeling parameters of  $L_R$ ,  $L_M$ ,  $n$  are calculated as given in (15, 16, 17)

$$L_R = (1 - k^2)L_{Tx} \quad (15)$$

$$L_M = k^2L_{Tx} \quad (16)$$

$$n = k\sqrt{\frac{L_{Tx}}{L_{Rx}}} \quad (17)$$

The system quality factor ( $Q$ ) should be high enough to make the FHA valid.  $Q$  depends on the Rx-side self-inductance ( $L_{Rx}$ ) and load resistance  $R_{Rx}$ , which can be calculated as in (18). Besides, for higher quality factors, the system gain decreases sharply when the operation frequency moves away from the resonant frequency.

$$Q = L_{Rx} \frac{2\pi f_r}{R_{Rx}} \quad (18)$$

### B. Design Steps

The design procedure starts with determining input/output voltage and power ratings. The VCPSM generates the input voltage, which can be calculated as in (19).

$$U_i = \hat{S}_{ABf_s} V_{DC} \quad (19)$$

The field winding ratings specify the output voltage and the load resistance in the transformer model. The reflected (load) resistance ( $R_{Rx}$ ) and voltage ( $U_o$ ) values are calculated as in (20) and (21)

$$U_o = \frac{2\sqrt{2}}{\pi} U_F \quad (20)$$

$$R_{Rx} = \frac{8}{\pi^2} R_F \quad (21)$$

where  $R_F$  is the resistance of the field winding and  $U_F$  is the applied voltage of the field winding.

Later on, it is required to select the quality factor, which determines the frequency control bandwidth. In the literature,  $Q$  is selected between 2 and 10 as a rule of thumb [40], [41]. After that,  $L_{Rx}$  is calculated by (18), where the resonant frequency is selected close to the switching frequency of the motor drive. Besides, it is needed to select the coupling coefficient, which can be practically achieved up to 0.8. Then,  $L_{Tx}$  can be calculated as in (22).

$$L_{Tx} = \frac{n^2}{k^2} L_{Rx} = \frac{U_i^2}{U_o^2} \frac{L_{Rx}}{k^2} \quad (22)$$

Lastly, the compensation capacitance can be calculated as given in (23). The gain at the resonant frequency does not directly depend on the capacitance value, but it just shifts the resonant frequency as shown in Fig. 11. Upon calculations above, the designed parameters of the SN-WPT system are shown in Table I.

$$C_{Tx} = \frac{1}{2\pi f_r \sqrt{L_R}} \quad (23)$$

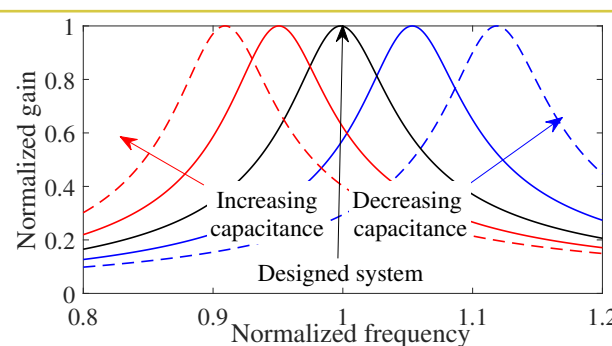


Fig. 11. The normalized gain over the normalized frequency of SN-WPT system for varying capacitance ( $C_{Tx}$ )

## V. EXPERIMENTAL VALIDATION

An experimental setup consisting of a 3-phase 3-wire GaN-based inverter and an SN-compensated WPT-based contactless field excitation system is established, as shown in Fig. 12. Table I presents the WPT system parameters achieved in the experimental setup. They are slightly different from the designed parameters due to the manufacturing tolerances.

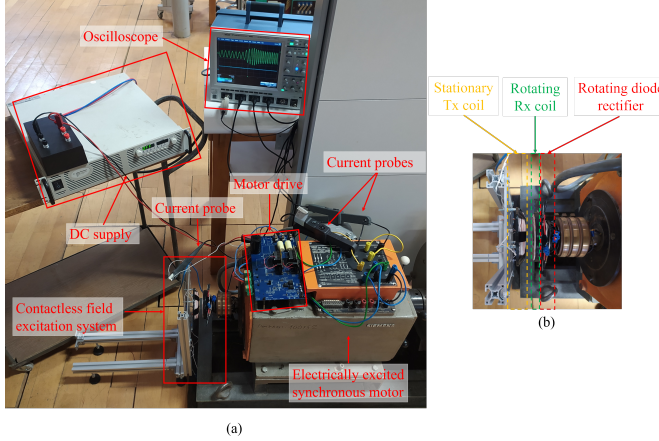


Fig. 12. Experimental setup. a) Overall view. b) Close view of the CFE system.

TABLE I  
THE MOTOR DRIVE SPECIFICATIONS, FIELD WINDING SPECIFICATIONS AND THE WPT SYSTEM PARAMETERS

Motor Drive Specifications		
DC-link Voltage ( $V_{DC}$ )	100 V	
Modulation Index ( $m_a$ )	0 – 0.8	
Normalized input voltage ( $\hat{S}_{ABf_s}$ )	0.44	
Switching frequency ( $f_s$ )	60 kHz	

Field Winding Specifications		
Field Inductance ( $L_F$ )	5 mH	
Field Resistance ( $R_F$ )	1.2 Ω	
Field Current ( $I_F$ )	5 A	
Field Voltage ( $U_F$ )	6 V	

WPT System Parameters	Designed	Experimental
Tx Inductance ( $L_{Tx}$ )	1500 μH	1510 μH
Rx Inductance ( $L_{Rx}$ )	8 μH	7.3 μH
Mutual Inductance ( $M$ )	50 μH	55.4 μH
Tx Capacitance ( $C_{Tx}$ )	5.9 nF	5.2 nF

Firstly, the proposed method is tested to validate the mathematical model. Secondly, the field excitation system is tested under several operating conditions of the fundamental frequency, modulation index, and switching frequency. Finally, the proposed CFE system is concurrently operated with the EESM.

### A. Input Excitation Voltage of the VSI

The voltage waveform between phase A and phase B is measured while SPWM is applied in different modulation indices. The normalized voltage waveform and its decomposition of the switching harmonic are shown in Fig. 13 for different modulation indices. It is observed that a constant input excitation at 0.44 normalized gain is achieved until the modulation index of 0.8. The value starts fluctuating in higher

modulation indices, after which is named the uncontrollable region. However, there is also a small fluctuation in the controllable region, and it can be ignored since it is under 5% of 0.44.

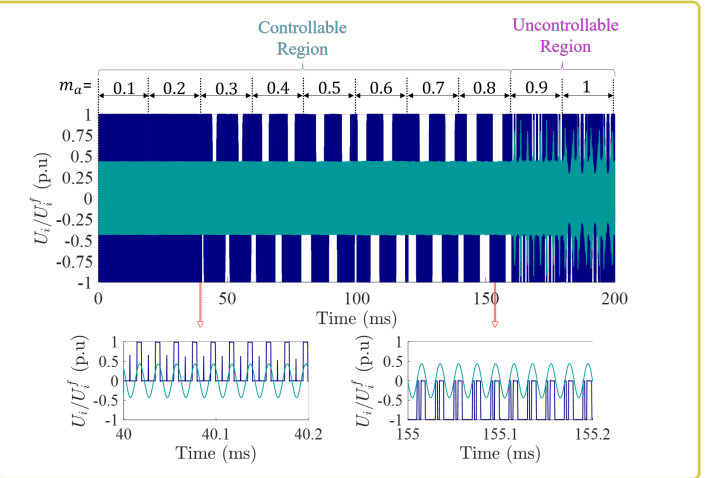


Fig. 13. The normalized voltage waveform of  $U_i$  and its decomposition of the switching frequency components  $U_i^f$  for different modulation indices.

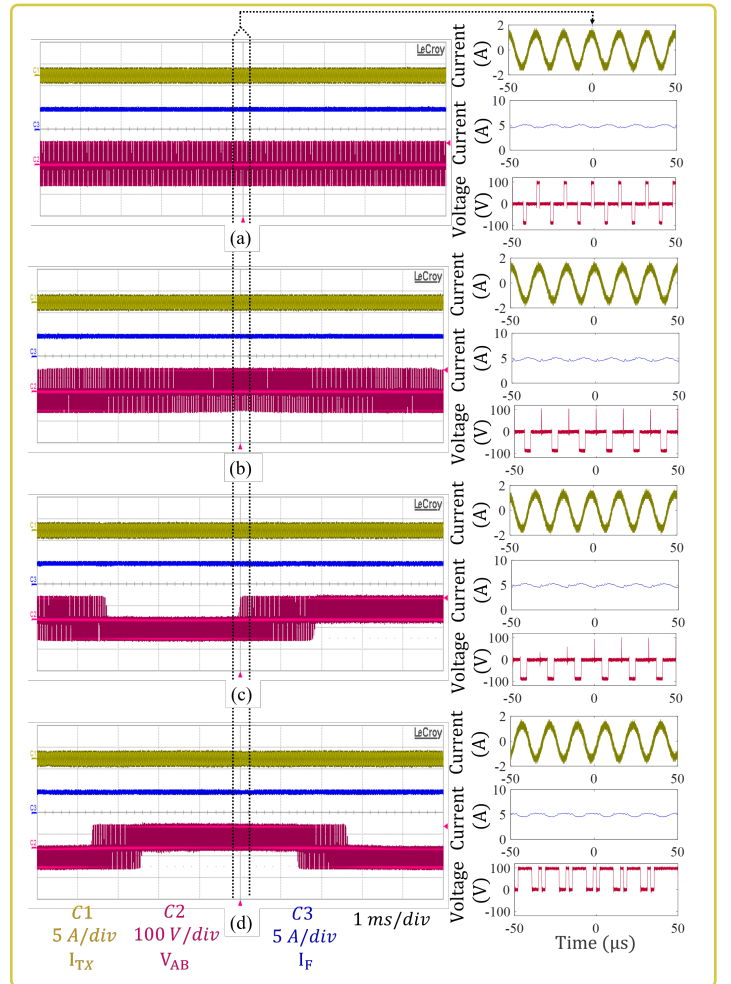


Fig. 14. The field current, Tx current, and input excitation voltage along several modulation indices under constant fundamental and switching frequency. a)  $m_a = 0$ . b)  $m_a = 0.25$ . c)  $m_a = 0.5$ . d)  $m_a = 0.75$ .

### B. The Wireless Power Transfer System

The WPT system is connected between phase A and phase B, like the previous test. The output of the WPT system is connected to the field of the EESM, but the phases of the EESM are not excited, which is equivalent to a stationary machine. Firstly, the DC-link voltage and fundamental frequency are adjusted to 100 V and 100 Hz. The field current, Tx current, and input excitation voltage are measured for several modulation indices in the controllable region, as presented in Fig. 14. The mean currents of the field winding for the modulation index of 0, 0.25, 0.5, and 0.75 were measured at 4.83 A, 4.72 A, 4.95 A, and 4.93 A, respectively. Therefore, it is concluded that an almost constant field current can be achieved while changing the modulation index. These minor differences (maximum 5%) can be compensated by detuning the switching frequency, which will be discussed.

Secondly, the modulation index is kept at 0.6, and the fundamental frequency alters to 100 Hz from 200 Hz. The field current, Tx current, and input excitation voltage are given in Fig 15. Accordingly, it is monitored that the field current is not affected by the fundamental frequency.

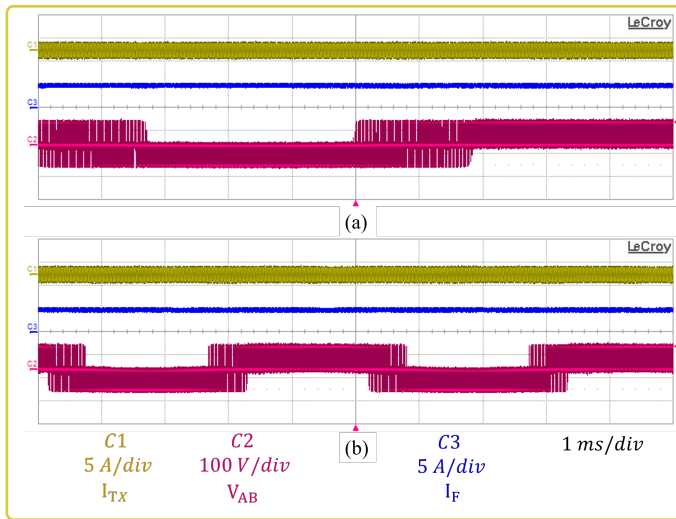


Fig. 15. The field current, Tx current, and input excitation voltage for fundamental frequencies of 100 Hz and 200 Hz under constant switching frequency and modulation index. a) 100 Hz. b) 200 Hz.

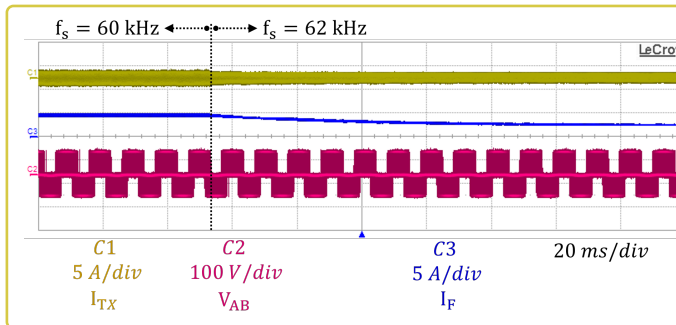


Fig. 16. The field current, Tx current, and input excitation voltage for switching frequencies of 60 kHz and 62 kHz under constant fundamental frequency and modulation index.

Lastly, the modulation index and fundamental frequency are kept at 0.6 and 100 Hz. As presented in Fig. 16, the switching frequency is altered to 60 kHz from 62 kHz. In this case, the field current decreases from 5 A to 2.5 A. Hence, it is achieved that the field current could be regulated by the hybrid frequency detuning method.

### C. Concurrent Operation of the CFE System and EESM

In this test, the phases of the EESM are also excited in addition to the field winding. The speed of EESM is increased from 52 RPM to 101 RPM. The phase A current of the EESM and the field current are given in Fig. 17. Accordingly, it is observed that the change in the motor speed minorly affects the field current. The minor changes can be compensated by detuning the switching frequency, as discussed before.

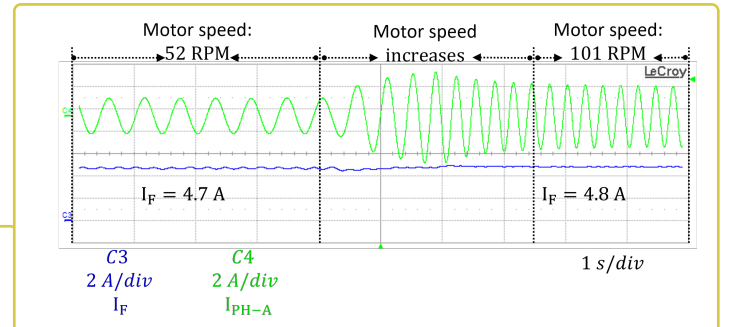


Fig. 17. The field and phase currents while motor speed increases from 52 RPM to 101 RPM.

### D. Effect of VCPSM on the Stator Current

The proposed VCPSM utilizes the magnitude of the first switching frequency for the field current control. Therefore, the proposed system generates higher effective voltage harmonics than conventional SPWM, but the high phase inductance filters out these harmonics at the stator current. An exception would be motors with low inductance, such as air-cored machines, where the voltage harmonics may lead to increase current and torque ripples.

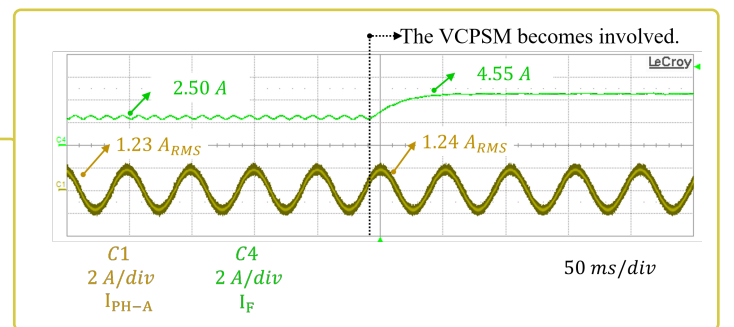


Fig. 18. The effect of the VCPSM on the stator current.

An RL load with an impedance equal to the stator winding is used in this test since the field windings could not be appropriately excited without the proposed method, causing an improper motor operation. The test is initialized using conventional SPWM, which generates uncontrolled sideband and

switching frequency. The field and stator currents measured as  $2.5 \text{ A}$  and  $1.23 \text{ A}_{\text{RMS}}$ , also seen in Fig. 18. Then, the proposed method is employed. The field current achieved the desired magnitude of  $4.55 \text{ A}$  without a low-frequency ripple. Moreover, it is observed that the stator current remains constant throughout this test, as expected.

#### E. Dynamic Performance of the VCPSM

A step change in the reference of the field current (i.e., the output of the WPT system) is applied to evaluate the dynamic performance of the proposed method, as shown in Fig. 19. At  $t_1$ ,  $I_F$  reference is changed, and  $I_{\text{PH-A}}$  is deviated due to this change. At  $t_2$ ,  $I_F$  is settled. At  $t_3$ , the controller brings  $I_{\text{PH-A}}$  to the previous value. Although the controller is not fully optimized, it is observed that the overshoot of the system is acceptable, and the steady-state error is negligible.

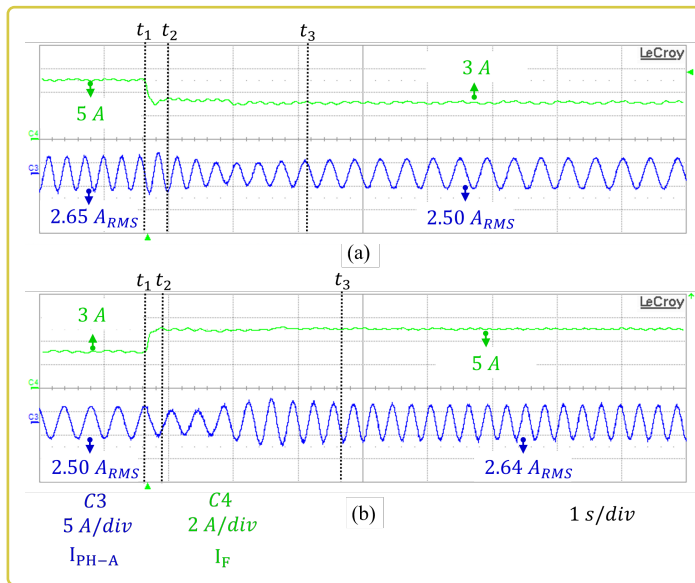


Fig. 19. Dynamic performance of the stator current. a) Field current decreases. b) Field current increases.

#### F. Effect of the VCPSM on the Efficiency

The losses of the motor drive were measured with and without the proposed method for the same modulation index and fundamental current, as presented in Table II. The input power increases when the proposed method is employed since the motor drive also excites the field winding. A minor increase in drive losses is observed. This increase causes the efficiency to decrease a little, but this efficiency decrease is negligible.

TABLE II  
EFFECT OF THE VCPSM ON THE MOTOR DRIVE LOSSES AND EFFICIENCY

Conventional SPWM (Only Stator Excitation)			
Input Power	Output Power	Losses	Efficiency (%)
318 W	302 W	16 W	94.97
The Proposed VCPSM (Both Stator and Field Excitation)			
Input Power	Output Power	Losses	Efficiency (%)
355 W	335 W	20 W	94.37

#### VI. CONCLUSION

This article proposes a novel wireless power transfer-based contactless field excitation system that can be integrated into conventional electrically excited synchronous motors. Unlike traditional systems, the proposed method utilizes the existing motor drives and does not require extra converters on both the Tx and Rx sides, reducing the cost and complexity. This study also presents a novel variable carrier phase shift method for independent control of the field and phase current while using conventional PWM methods. However, the proposed method does not control the field current to the full range. It only guarantees a constant excitation voltage for different modulation indices. Therefore, a hybrid control strategy consisting of the VCPSM and frequency detuning methods is also presented to regulate field current. A prototype with a 3-phase GaN-based motor drive with 100 V DC-link and 60 kHz switching frequency was established to validate the proposed system. It was observed that the input excitation of the WPT system is kept constant at 44 V peak, which also means that the field current is kept almost constant at 5 A while changing the modulation index. Also, it was achieved that the field current was reduced from 5 A to 2.5 A by detuning the switching frequency. Further, it was experimentally observed that the proposed system has a negligible effect on the stator current and drive efficiency. Consequently, a cost-reduced CFE system for EESMs is achieved by only updating the control algorithm without using active converters.

#### REFERENCES

- C. H. T. Lee, W. Hua, T. Long, C. Jiang, and L. V. Iyer, "A critical review of emerging technologies for electric and hybrid vehicles," *IEEE Open Journal of Vehicular Technology*, vol. 2, pp. 471–485, 2021.
- A. Naina, S. Paryani, and S. S. N. Jani, "Comparison between surface-mounted and interior pm motor for ev application," in *2021 International Conference on Intelligent Technologies (CONIT)*, 2021, pp. 1–6.
- H. Huang, Y.-S. Hu, Y. Xiao, and H. Lyu, "Research of parameters and antide magnetization of rare-earth-less permanent magnet-assisted synchronous reluctance motor," *IEEE Transactions on Magnetics*, vol. 51, no. 11, pp. 1–4, 2015.
- D. G. Dorrell, "Are wound-rotor synchronous motors suitable for use in high efficiency torque-dense automotive drives?" in *IECON 2012 - 38th Annual Conference on IEEE Industrial Electronics Society*, 2012, pp. 4880–4885.
- I. Boldea, L. N. Tutelea, L. Parsa, and D. Dorrell, "Automotive electric propulsion systems with reduced or no permanent magnets: An overview," *IEEE Transactions on Industrial Electronics*, vol. 61, no. 10, pp. 5696–5711, 2014.
- F. Grafeo, S. Vaschetto, M. Cossale, M. Kerschbaumer, E. C. Bortoni, and A. Cavagnino, "Cylindrical wound-rotor synchronous machines for traction applications," in *2020 International Conference on Electrical Machines (ICEM)*, vol. 1, 2020, pp. 1736–1742.
- A. Di Gioia, I. P. Brown, Y. Nie, R. Knippel, D. C. Ludois, J. Dai, S. Hagen, and C. Alteheld, "Design and demonstration of a wound field synchronous machine for electric vehicle traction with brushless capacitive field excitation," *IEEE Transactions on Industry Applications*, vol. 54, no. 2, pp. 1390–1403, 2018.
- Y. Kim and K. Nam, "Copper-loss-minimizing field current control scheme for wound synchronous machines," *IEEE Transactions on Power Electronics*, vol. 32, no. 2, pp. 1335–1345, 2017.
- J. K. Skjølberg, H. F. Ohma, and M. Runde, "Wear rates and current distribution of carbon brushes on steel slip rings," *IEEE Transactions on Energy Conversion*, vol. 24, no. 4, pp. 835–840, 2009.
- J. K. Nøland, F. Evestedt, J. J. Pérez-Loya, J. Abrahamsson, and U. Lundin, "Testing of active rectification topologies on a six-phase rotating brushless outer pole pm exciter," *IEEE Transactions on Energy Conversion*, vol. 33, no. 1, pp. 59–67, 2018.

- [11] A. Di Gioia, I. P. Brown, Y. Nie, R. Knippel, D. C. Ludois, J. Dai, S. Hagen, and C. Alteheld, "Design of a wound field synchronous machine for electric vehicle traction with brushless capacitive field excitation," in *2016 IEEE Energy Conversion Congress and Exposition (ECCE)*, 2016, pp. 1–8.
- [12] S. Hagen, M. Tisler, J. Dai, I. P. Brown, and D. C. Ludois, "Use of the rotating rectifier board as a capacitive power coupler for brushless wound field synchronous machines," *IEEE Journal of Emerging and Selected Topics in Power Electronics*, vol. 10, no. 1, pp. 170–183, 2022.
- [13] J. Tang, Y. Liu, and N. Sharma, "Modeling and experimental verification of high-frequency inductive brushless exciter for electrically excited synchronous machines," *IEEE Transactions on Industry Applications*, vol. 55, no. 5, pp. 4613–4623, 2019.
- [14] D. C. Ludois, J. K. Reed, and K. Hanson, "Capacitive power transfer for rotor field current in synchronous machines," *IEEE Transactions on Power Electronics*, vol. 27, no. 11, pp. 4638–4645, 2012.
- [15] J. Dai, S. Hagen, D. C. Ludois, and I. P. Brown, "Synchronous generator brushless field excitation and voltage regulation via capacitive coupling through journal bearings," *IEEE Transactions on Industry Applications*, vol. 53, no. 4, pp. 3317–3326, 2017.
- [16] A. M. Lulhe and T. N. Date, "A technology review paper for drives used in electrical vehicle (ev) hybrid electrical vehicles (hev)," in *2015 International Conference on Control, Instrumentation, Communication and Computational Technologies (ICCI CCT)*, 2015, pp. 632–636.
- [17] S. Tiwari, O.-M. Midtgård, and T. M. Undeland, "Sic mosfets for future motor drive applications," in *2016 18th European Conference on Power Electronics and Applications (EPE'16 ECCE Europe)*, 2016, pp. 1–10.
- [18] B. Wrzecionko, D. Bortis, and J. W. Kolar, "A 120 °C ambient temperature forced air-cooled normally-off sic jfet automotive inverter system," *IEEE Transactions on Power Electronics*, vol. 29, no. 5, pp. 2345–2358, 2014.
- [19] J. Millán, P. Godignon, X. Perpiñà, A. Pérez-Tomás, and J. Rebollo, "A survey of wide bandgap power semiconductor devices," *IEEE Transactions on Power Electronics*, vol. 29, no. 5, pp. 2155–2163, 2014.
- [20] J. Dai, S. Hagen, D. C. Ludois, and I. P. Brown, "Synchronous generator brushless field excitation and voltage regulation via capacitive coupling through journal bearings," *IEEE Transactions on Industry Applications*, vol. 53, no. 4, pp. 3317–3326, 2017.
- [21] D. C. Ludois, M. J. Erickson, and J. K. Reed, "Aerodynamic fluid bearings for translational and rotating capacitors in noncontact capacitive power transfer systems," *IEEE Transactions on Industry Applications*, vol. 50, no. 2, pp. 1025–1033, 2014.
- [22] D. Maier, J. Kurz, and N. Parspour, "Contactless energy transfer for inductive electrically excited synchronous machines," in *2019 IEEE PEWS Workshop on Emerging Technologies: Wireless Power Transfer (WoW)*, 2019, pp. 191–195.
- [23] L. Sun, J. Kang, Y. Liu, Z. Mao, and Z. Zhong, "Wireless power transfer based contactless excitation of electrically excited synchronous motor," in *2020 IEEE 9th International Power Electronics and Motion Control Conference (IPEMC2020-ECCE Asia)*, 2020, pp. 1091–1097.
- [24] X. Feng, Z. Fu, G. Hao, K. Wang, and Y. Weng, "Modeling and implementation of a new non-contact slip ring for wireless power transfer," in *2020 IEEE 9th International Power Electronics and Motion Control Conference (IPEMC2020-ECCE Asia)*, 2020, pp. 106–111.
- [25] K. Song, B. Ma, G. Yang, J. Jiang, R. Wei, H. Zhang, and C. Zhu, "A rotation-lightweight wireless power transfer system for solar wing driving," *IEEE Transactions on Power Electronics*, vol. 34, no. 9, pp. 8816–8830, 2019.
- [26] R. Trevisan and A. Costanzo, "A 1-kw contactless energy transfer system based on a rotary transformer for sealing rollers," *IEEE Transactions on Industrial Electronics*, vol. 61, no. 11, pp. 6337–6345, 2014.
- [27] C. Zhang, D. Lin, and S. Y. R. Hui, "Ball-joint wireless power transfer systems," *IEEE Transactions on Power Electronics*, vol. 33, no. 1, pp. 65–72, 2018.
- [28] E. Ayaz, O. Altun, H. Polat, F. Karakaya, and O. Keysan, "Concurrent wireless power transfer and motor drive system with a single converter," *IEEE Journal of Emerging and Selected Topics in Industrial Electronics*, pp. 1–9, 2022.
- [29] X. Qu, H. Chu, S. C. Wong, and C. K. Tse, "An ipt battery charger with near unity power factor and load-independent constant output combating design constraints of input voltage and transformer parameters," *IEEE Transactions on Power Electronics*, vol. 34, no. 8, pp. 7719–7727, 2019.
- [30] X. Qu, H. Chu, S.-C. Wong, and C. K. Tse, "An ipt battery charger with near unity power factor and load-independent constant output combating design constraints of input voltage and transformer parameters," *IEEE Transactions on Power Electronics*, vol. 34, no. 8, pp. 7719–7727, 2019.
- [31] Y. H. Sohn, B. H. Choi, E. S. Lee, G. C. Lim, G.-H. Cho, and C. T. Rim, "General unified analyses of two-capacitor inductive power transfer systems: Equivalence of current-source ss and sp compensations," *IEEE Transactions on Power Electronics*, vol. 30, no. 11, pp. 6030–6045, 2015.
- [32] D. G. Holmes and T. A. Lipo, "Pulse width modulation for power converters," *IEEE Press*, 2003.
- [33] Z. Pantic, K. Lee, and S. M. Lukic, "Multifrequency inductive power transfer," *IEEE Transactions on Power Electronics*, vol. 29, no. 11, pp. 5995–6005, 2014.
- [34] C. Zhao and D. Costinett, "Gan-based dual-mode wireless power transfer using multifrequency programmed pulse width modulation," *IEEE Transactions on Industrial Electronics*, vol. 64, no. 11, pp. 9165–9176, 2017.
- [35] C. Xia, N. Wei, H. Zhang, S. Zhao, Z. Li, and Z. Liao, "Multifrequency and multiload mcr-wpt system using hybrid modulation waves spwm control method," *IEEE Transactions on Power Electronics*, vol. 36, no. 11, pp. 12400–12412, 2021.
- [36] J. Wu, L. Bie, W. Kong, P. Gao, and Y. Wang, "Multi-frequency multi-amplitude superposition modulation method with phase shift optimization for single inverter of wireless power transfer system," *IEEE Transactions on Circuits and Systems I: Regular Papers*, vol. 68, no. 5, pp. 2271–2279, 2021.
- [37] Y. Liu, C. Liu, X. Gao, and S. Liu, "Design and control of a decoupled multichannel wireless power transfer system based on multilevel inverters," *IEEE Transactions on Power Electronics*, vol. 37, no. 8, pp. 10045–10060, 2022.
- [38] E. Ayaz, O. Altun, and O. Keysan, "Carrier phase shift method of spwm for concurrent wired and wireless power transfer systems," *IEEE Transactions on Industrial Electronics*, pp. 1–10, 2022.
- [39] Y. Zhang, T. Kan, Z. Yan, Y. Mao, Z. Wu, and C. C. Mi, "Modeling and analysis of series-none compensation for wireless power transfer systems with a strong coupling," *IEEE Transactions on Power Electronics*, vol. 34, no. 2, pp. 1209–1215, 2019.
- [40] G. A. Covic and J. T. Boys, "Modern trends in inductive power transfer for transportation applications," *IEEE Journal of Emerging and Selected Topics in Power Electronics*, vol. 1, no. 1, pp. 28–41, 2013.
- [41] K. Aditya and S. S. Williamson, "Design guidelines to avoid bifurcation in a series-series compensated inductive power transfer system," *IEEE Transactions on Industrial Electronics*, vol. 66, no. 5, pp. 3973–3982, 2019.